COLLOIDAL CRYSTALLIZATION BETWEEN TWO AND THREE DIMENSIONS

H. LÖWEN, E. C. OĞUZ, L. ASSOUD, and R. MESSINA

Institut für Theoretische Physik II: Weiche Materie, Heinrich-Heine-Universität Düsseldorf, D-40225 Düsseldorf, Germany

CONTENTS

I.   INTRODUCTION

Predicting the stable crystalline structure for a given material is one of the fundamental problems in condensed matter science, metallurgy, chemistry, and mechanical engineering [1]. Even if the basic interparticle interactions stem from a pairwise potential $V(r)$ that solely depends on the interparticle distance r, there are a variety of different stable crystalline lattices for different shapes of the

potential $V(r)$ [2]. To name just a few examples in three dimensions, there are face-centered cubic crystals for strong repulsions (like hard spheres) and body-centered cubic crystals of soft repulsions (like point charges) [3–5], cluster and anisotropic solids for penetrable potentials [6, 7], and isostructural solid–solid transitions for square-well and square-shoulder potentials [8–11]. This complicated problem is a bit more transparent in two spatial dimensions, that is, for particles in the plane, where less lattice types exist than those in three dimensions [12]. Nevertheless, even for a planar monolayer, the resulting periodic structure is not understood completely. In most but not all cases, a triangular (or hexagonal) crystal turns out to be stable corresponding to the close-packing limit of hard disks. The two-dimensional Wigner crystal for classical point-like electrons in a plane [13] has the same triangular lattice but more structured and nondivergent interaction potentials can lead to stable lattices different from the triangular one. Strictly speaking, long-range spatial periodicity exists only at zero temperature in two dimensions [14].

The situation is much more complex for binary mixtures characterized by a set of pairwise interactions, $V_{AA}(r)$, $V_{AB}(r) = V_{BA}(r)$, $V_{BB}(r)$, where the subscript refers to the species that interact. For mixtures of hard disks, already there is a wealth of close-packed [15] and thermodynamically stable [16] binary crystalline structures. Hence, it becomes clear that a further species opens the way for a new class of complex composite crystals that need to be understood better for various explicit forms of the interaction potentials.

Another way of increasing complexity significantly is to stick to a one-component system but open the third dimension, that is, switch from a monolayer of crystalline particles toward bi- and multilayers. This can be realized, for example, by weakening the confinement conditions. Some of the particles will explore the spatial coordinate perpendicular to the monolayer and new structures emerge. For the close-packed structure of hard spheres confined between two parallel hard plates, there is a zigzag buckling ending up in a staggered bilayer of two intersecting square monolayers, if the distance between the two confining plates is increased. Upon further widening of the slit width, the square bilayer structure is followed by rhombic bilayers and two intercalating triangular layers [17–19]. This already demonstrates that complex structures emerge if the third coordinate comes into play.

In this chapter, we review recent progress made to predict the crystalline layer structure between two and three dimensions. Both the planar two-component case and the one-component multilayered case will be treated consecutively. This will be done mainly for simple models relevant for colloidal dispersions, granular matter, and dusty plasma sheets [20]. Most considerations focus on the ground state; that is, we are considering zero temperature.

II. FREEZING OF BINARY SYSTEMS IN TWO SPATIAL DIMENSIONS

A. Binary Mixtures of Hard Disks

The maybe simplest nontrivial system for a two-dimensional binary mixtures is that of hard disks where temperature scales out since everything is governed by entropy. This is a reasonable model for sterically stabilized colloidal mixtures that are pending at an interface. More explicitly, the pair potential reads

$$V_{\alpha\beta}^{HS}(r) = \begin{cases} 0 & \text{if } r \geq R_\alpha + R_\beta \;\; (\alpha, \beta = A, B) \\ \infty & \text{if } r < R_\alpha + R_\beta \end{cases} \tag{1}$$

where R_A and R_B denote the two additive radii of the two species, with $A(B)$ referring to the big (small) disks. The first question to answer is the close-packing configuration of hard-disk mixtures and the corresponding stable crystalline structures. For close packing, the phase diagram was calculated in Ref. [15]. For small asymmetries, there is a complete phase separation into two pure A and B crystals, while more complicated mixed crystals are getting stable at higher asymmetry. The stability of most of the phases was recently confirmed at finite pressure [16].

B. Binary Mixtures of Parallel Dipoles

Superparamagnetic colloidal particles pending at an air–water interface are an excellent realization of two-dimensional classical many-body systems [21–25]. The system can also be prepared by using binary particles with small and large (permanent) dipole moments [26–29]. A strong enough external magnetic field B_0 perpendicular to the air–water interface induces parallel dipole moments (m_A, m_B) in the A and B particles, resulting in an effective repulsive interaction that scales as the inverse cube of the particle separation r within the interface. Defining the magnetic susceptibilities as $\chi_{A/B} = m_{A/B}/B_0$, the pair potentials read

$$V_{\alpha\beta}(r) = \frac{\mu_0}{4\pi} \chi_\alpha \chi_\beta B_0^2 / r^3 \quad (i, j = A, B) \tag{2}$$

where μ_0 represents the vacuum permeability. Note that since the induced dipole moment is linear in the external field, χ_α is field independent for low B_0.

Then, the strength of the external magnetic field corresponds to an inverse temperature. Therefore, these systems are similar to ferrofluids [30–32]. Indeed, for this inverse power potential, at fixed composition and susceptibility ratio,

$m \equiv m_B/m_A = \chi_B/\chi_A$, all static quantities solely depend [33] on a dimensionless interaction strength (or coupling constant)

$$\Gamma = \frac{\mu_0}{4\pi} \frac{\chi_A^2 B_0^2}{k_B T a^3} \tag{3}$$

where $k_B T$ is the thermal energy at room temperature and $a = 1/\sqrt{\rho_A}$ the average interparticle separation between A particles.

Another realization is a mixture of granular spheres in an external magnetic field. Different granulate materials will lead to different dipole moments such that a dipolar mixture is realized [34]. Typically, granulates are put on a horizontal vibrating table. For small enough vibration strengths, the system is expected to be close to the equilibrium ground state of zero temperature.

At zero temperature (i.e., $\Gamma \to \infty$), the state of the binary system is completely described by the ratio $0 \leq m \leq 1$ of the two dipole moments and the relative composition X of the second species (B) with smaller dipole moment. The two-dimensional phase diagram of the mixture in the (m, X) plane was calculated at zero temperature via lattice sum minimization in Ref. [35]. The result is shown in Fig. 1. A wealth of different stable phases is found to be stable that is getting increasingly more complex with increasing asymmetry [36]. Details of the crystalline structures found are summarized and explained in Fig. 2 and Table I.

For small asymmetries m and intermediate compositions X, the system splits into triangular phases A_2B and AB_2 in marked contrast to the hard-disk
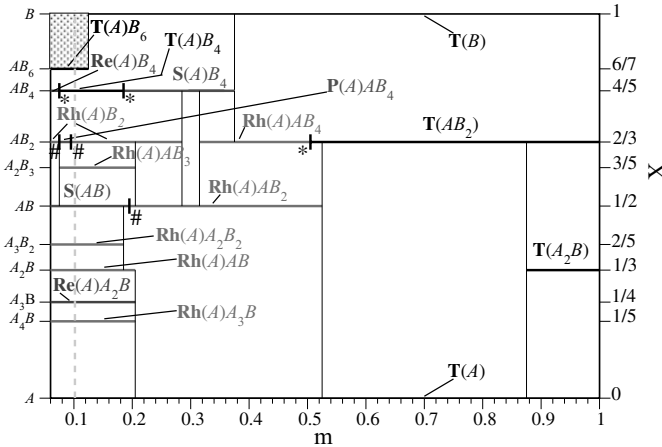

Figure 1. The phase diagram in the (m, X) plane of dipolar asymmetry m and composition X at $T = 0$. The gray box indicates an unknown region. The symbol # (∗) denotes continuous (discontinuous) transitions. Adapted from Ref. [35]. (See the color version of this figure in Color Plates section.)
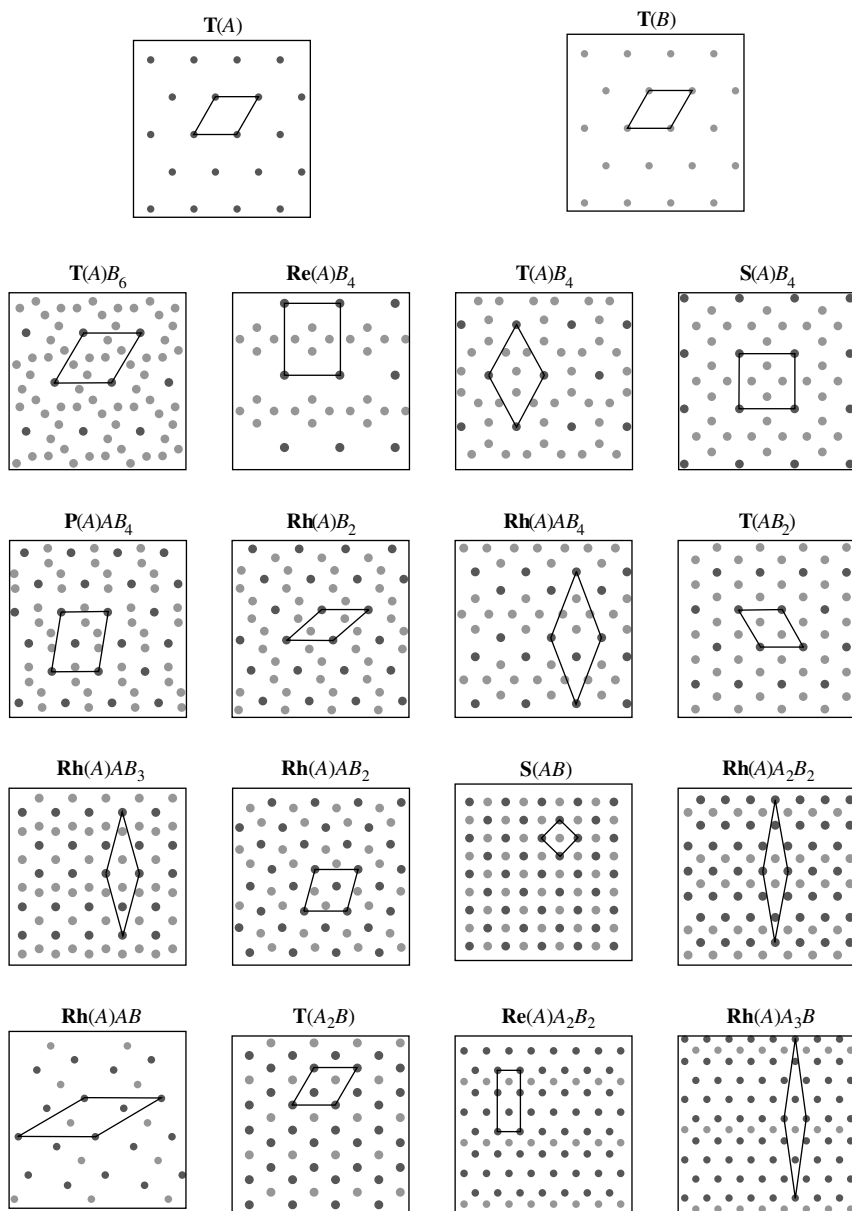
Figure 2.   The stable binary crystal structures and their primitive cells. The red dark (green light) disks correspond to A (B) particles. Adapted from Ref. [35]. (See the color version of this figure in Color Plates section.)

TABLE I
The Stable Phases with Their Bravais Lattice and Basis

Phase	Bravais Lattice (basis)
$\mathbf{T}(A)$	Triangular for A (one A particle)
$\mathbf{T}(B)$	Triangular for B (one B particle)
$\mathbf{S}(AB)$	Square for A and B together
	(one A and one B particle)
$\mathbf{S}(A)B_n$	Square for A
	(one A and n B particles)
$\mathbf{Re}(A)A_mB_n$	Rectangular for A
	$((m+1)$ A and n B particles)
$\mathbf{Rh}(A)A_mB_n$	Rhombic for A
	$((m+1)$ A and n B particles)
$\mathbf{P}(A)AB_4$	Parallelogram for A
	(two A and four B particles)
$\mathbf{T}(AB_2)$	Triangular for A and B together
	(one A and two B particles)
$\mathbf{T}(A_2B)$	Triangular for A and B together
	(two A and one B particle)
$\mathbf{T}(A)B_n$	Triangular for A
	(one A and n B particles)

mixture [15] that does not exhibit such a phase separation but just demixes into two pure triangular A and B crystals. The intermediate AB_2 structure has been confirmed by experiments on binary granular matter in two dimensions, which were also dominated by dipolar interactions [34].

Experiments on colloidal dipolar mixtures were performed for a strong asymmetry of $m = 0.1$. In the fluid state, pair correlations do agree with the dipolar model [37]. Regarding the crystalline states, almost all predicted phases were discovered in real-space experiments [38] but only as small crystallite patches and not as large bulk phases. This gives motivation to consider the nonequilibrium dynamics during quenching of the systems from a fluid deep into the crystalline state [39].

In fact, the magnetic field can almost instantaneously be changed on the diffusive timescale of motion of the colloidal particle [39]. Since formally the strength of the magnetic field corresponds to temperature, this represents an ultrafast temperature quench that is typically hard to realize in molecular systems. In Fig. 3, experimental two-dimensional snapshots of a colloidal mixture with $m = 0.1$ and $X = 0.4$ are shown. Before the quench, the system is exposed to a low magnetic field where the effective dimensionless coupling constant is $\Gamma = 1$, which is then changed to a high magnetic field where $\Gamma = 71$. Figure 3a shows the snapshot that is just after the quench while Fig. 3b shows the one that is after a time of 60τ, where
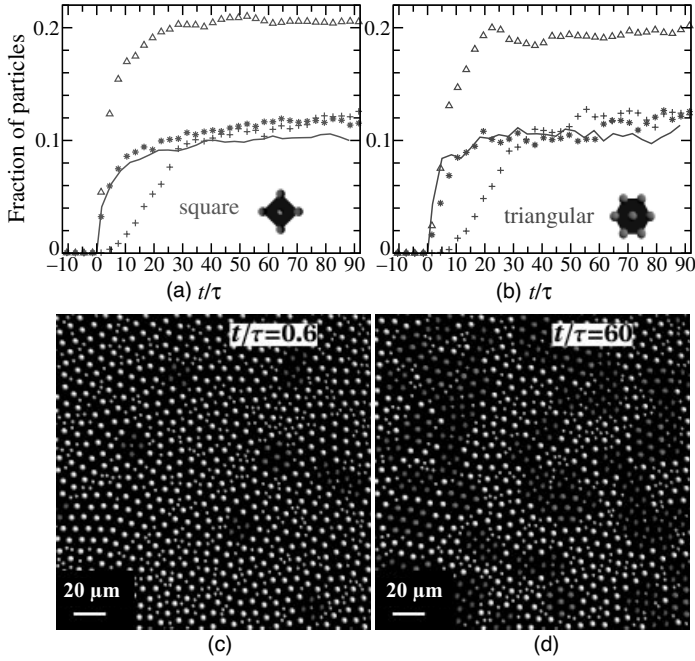
Figure 3. **(a)** Fraction of B particles belonging to a crystalline square surrounding (see inset) and **(b)** fraction of A particles belonging to a crystalline triangular surrounding (see inset) versus reduced time t/τ for an ultrafast quench from $\Gamma = 1$ to $\Gamma = 71$. The lines are experimental data while the symbols ($\ast$) are data from BD simulations. Two experimental snapshots for a time $t/\tau = 0.6$ just after the quench **(c)** and a later time $t/\tau = 60$ **(d)** are shown. Big particles are shown in blue if they belong to a triangular surrounding and in red if they belong to a square surrounding. All other big particles are shown in white color. Few big particles belonging to both triangular and square surroundings are shown in pink color. The small particles are shown in green if they belong to a square center of big particles, otherwise they appear in yellow. Also included are simulation data for an instantaneous "steepest descent" quench from $\Gamma = 1$ to $\Gamma = \infty$ ($\triangle$) and for a linear increase of Γ from $\Gamma = 1$ to $\Gamma = 71$ on a timescale of 30τ (+). Adapted from Ref. [39]. (See the color version of this figure in Color Plates section.)

τ is a convenient Brownian diffusive timescale for particle motion. Big particles with a triangular surrounding of other A particles are colored in blue while big particles with a square-like surrounding are colored in red. The fraction of blue and red colored particles increases with time as shown in Fig. 3 and reaches a saturation. Both experiments and Brownian dynamics computer simulation data are in agreement.

After the ultrafast quench, there is a nonmonotonic behavior in evolution of the partial pair distribution functions $g_{ij}(r)$, which are shown in Fig. 4 for three different times. Clearly, the amplitude in the first peak of $g_{BB}(r)$ exhibits a nonmonotonic
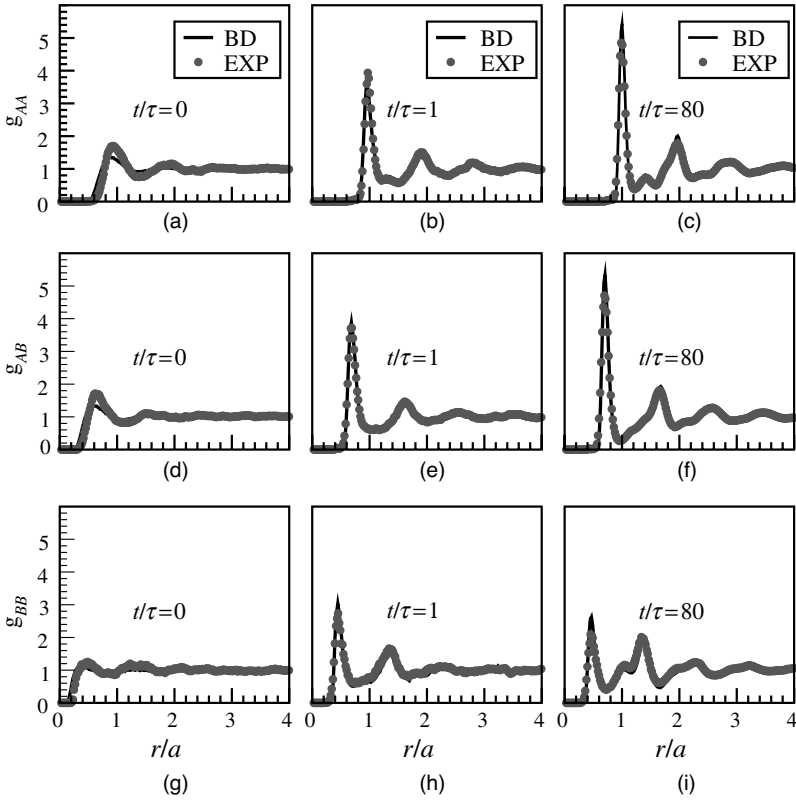
Figure 4. Partial pair distribution functions $g_{AA}(r)$, $g_{AB}(r)$, and $g_{BB}(r)$ of A and B particles versus reduced distance r/a at three different reduced times **(a)**, **(d)**, **(g)** ($t/\tau = 0$); **(b)**, **(e)**, **(h)** ($t/\tau = 1$); and **(c)**, **(f)**, **(i)** ($t/\tau = 80$). BD results (solid lines) are compared to experimental data (symbols). Adapted from Ref. [39]. (See the color version of this figure in Color Plates section.)

bahavior in time. For small times, the small particles are slaved to the big ones that are quickly moving to their energetically favorable positions. This gives rise to an increase in the peak height in $g_{BB}(r)$. Only on a larger timescale the smaller particles relax as well. This peculiar feature is again found in both experiment and Brownian dynamics computer simulations. Within the allotted time, the binary mixture does not find its true ground state as shown in Fig. 1 but is quenched to a "glass" with patches showing similarities to the stable bulk crystals. It is challenging to probe the dynamics in the patchy crystalline regions. In fact, the dynamics is significantly slower in the patchy crystalline regions than in the disordered parts. This might give a clue to understand at least parts of the dynamical heterogeneities in glasses [40–43].

C. Binary Yukawa Mixtures

While the dipole–dipole interactions are long range, charged suspensions confined between two charged plates are conveniently modeled by short-range screened Coulomb or Yukawa interactions [44–46], similar to that in three spatial dimensions [47]; for an experimental realization in the context of colloids, see Ref. [48]. Another realization of two-dimensional Yukawa particles are dusty plasma sheets [20]. Since the Yukawa interaction involves the screening length as an additional parameter, there is more freedom for topology of the phase diagram. The Yukawa model for a binary mixture is characterized by the pairwise potentials in detail:

$$V_{AA}(r) = V_0 \varphi(r), \quad V_{AB}(r) = V_0 Z \varphi(r),$$
$$V_{BB}(r) = V_0 Z^2 \varphi(r) \tag{4}$$

The dimensionless function $\varphi(r)$ is given by

$$\varphi(r) = \frac{\exp(-\kappa r)}{r} \tag{5}$$

where the energy amplitude V_0 sets the energy scale. In Debye–Hückel theory, the prefactor reads as $V_0 = Z_A^2 / 4\pi\epsilon_0\epsilon$, where ϵ is the dielectric permittivity of the solvent ($\epsilon = 1$ for the dusty plasma). Typically [49, 50], Z_A is on the order of 100–100,000 elementary charges, e, such that $V(r)/k_BT$ at interparticle distances $r = 1/\kappa$ equals $Z_A^2 \kappa \lambda_B / e^2$. Furthermore, the Bjerrum length $\lambda_B = e^2 / 4\pi\epsilon_0\epsilon k_BT$ is a few angstroms at room temperature and the Debye screening length, $1/\kappa$, is about a micrometer, such that $V(r)/k_BT$ is much larger than unity for high charges Z_A. This justifies formally zero-temperature calculations for the Yukawa particles. On the other hand, the screening microions possess a finite temperature that enters in the inverse Debye screening length κ.

In fact, the crystalline ground states have been addressed again by lattice sum minimization [51]. In the plane spanned by the charge asymmetry $Z = Z_B/Z_A$ and the composition X, phase diagrams for three different fixed pressures are presented in Fig. 5.

Similar to the extremely short-range hard-disk interactions, there is complete phase separation into pure A and B triangular crystals at small asymmetry where $Z \approx 1$. This is quite persistent over a broad range of asymmetries down to $Z \approx 0.5 - 0.6$. For higher asymmetries, the phase behavior is getting more complex. As a function of imposed pressure, at fixed charge asymmetry, there are more stable phases at higher pressure than at lower pressure. This has to do with the intuitive idea that small changes are more relevant for strong repulsion, that is, at higher pressure.
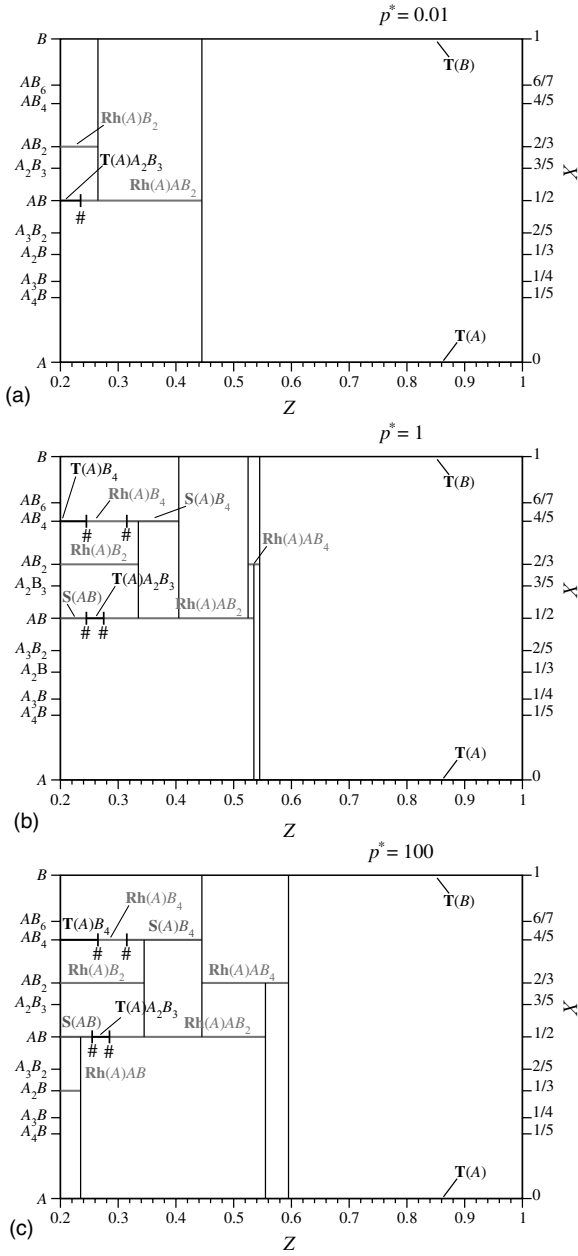
Figure 5. The phase diagram in the (Z, X) plane of charge asymmetry and composition at $T = 0$ for an effective pressure **(a)** $p^* = 0.01$, **(b)** $p^* = 1$, and **(c)** $p^* = 100$. The symbol # denotes a discontinuous transition. The y-axis is represented by two equivalent scales: the left-hand side indicates the phase symbols whereas the right-hand side shows the corresponding value of the composition. Adapted from Ref. [51]. (See the color version of this figure in Color Plates section.)

D.   Binary Mixtures of Oppositely Charged Particles with Different Sizes

As a final example, we discuss a two-component mixture of oppositely charged particles. To keep the model simple, there is no screening here, and the system is globally charge neutral. Both species carry the same magnitude of charge but opposite signs and the species possess a different hard-core radius R_α. Therefore, the binary pair potentials reads as

$$u_{\alpha\beta}(r) = \begin{cases} \frac{q_\alpha q_\beta}{4\pi\epsilon_0 r} & \text{if } r \geq R_\alpha + R_\beta \qquad (\alpha, \beta = A \text{ or } B) \\ \infty & \text{if } r < R_\alpha + R_\beta \end{cases} \tag{6}$$

where $q_A = -q_B = q$. A typical setup is to consider zero imposed pressure, that is, $P = 0$ [52, 53]. Then, again at zero temperature, one can find the minimum by a lattice sum minimization of the total potential free energy [54]. Owing to the hard-core part in the interaction, traditional minimizers fail to get to the correct minimum. An escape is the so-called penalty method [55], where the hard-sphere part is made penetrable without changing the minimum such that traditional minimization routine can be used.

Two setups have been considered in detail in Ref. [56], the "interfacial model" and "the substrate model," which are shown in Figs. 6 and 7. In the interfacial model, all centers of mass are confined to a common plane. This setup is designed for realizations where oppositely charged colloids [57] are confined to an interface [58]. On the substrate model, on the other hand, all particles are lying on the same plane. The latter is realized for granular metallic balls on a horizontal table. The granulates can be prepared with opposite charges [59–61].

In Fig. 6, the stable crystalline structures are presented as a function of the size asymmetry R_B/R_A for the interfacial model [56]. These structures minimize the potential energy per particle pair and are also classified according to their "connectivity" and coordination number. In particular, a "touching" configuration implies connecting big spheres and N_c measures the contacts between big and small spheres per big particle. By increasing the size asymmetry, the following cascade is found:

$$\triangle(\text{touching, } N_c = 2) \rightarrow \triangle(\text{touching, } N_c = 3) \rightarrow$$
$$\triangle(\text{nontouching, } N_c = 3) \rightarrow \text{Rh}(\text{touching, } N_c = 3) \rightarrow$$
$$\square(\text{touching, } N_c = 4) \rightarrow \square(\text{nontouching, } N_c = 4)$$

Here, $\triangle$ ($\square$) means a triangular (square) structure of the big particles and Rh denotes a rhombic cell (see Fig. 6).
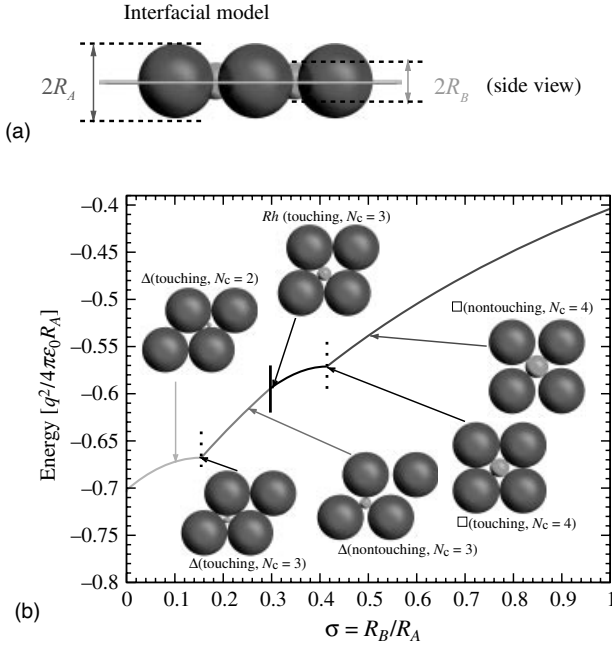
Figure 6. Stable structures of oppositely charged spheres versus their size asymmetry $\sigma = R_B/R_A$ in the interface model, where all sphere centers fall on the same plane: **(a)** side view, **(b)** energy per ion (scaled). The discontinuous transition is indicated by a solid bar. Continuous transitions are denoted by a broken bar. Unit cells of the corresponding stable phases are shown, where the big (small) have a radius R_A (R_B). (See the color version of this figure in Color Plates section.)

For the substrate model, on the other hand, the stable structures are shown in Fig. 7. The cascade now is

empty crystal of dipoles (nontouching, $N_c = 1$) →
empty crystal of chains (nontouching, $N_c = 1$) →
empty crystal of chains (touching, $N_c = 1$) →
empty crystal of chains (touching, $N_c = 2$) →
empty crystal of chains (nontouching, $N_c = 2$) →
△(nontouching, $N_c = 3$) → □(nontouching, $N_c = 4$)

Here, the notation "empty" means that at least one lattice constant is diverging. An empty chain crystal has one diverging distance between chains, whereas the empty dipole crystal has two diverging lattice constants.

Recent experiments on oppositely charged granular sheets with $\sigma \approx 1$ [59, 60] have indeed revealed a stable □(nontouching) configuration that is confirmed by
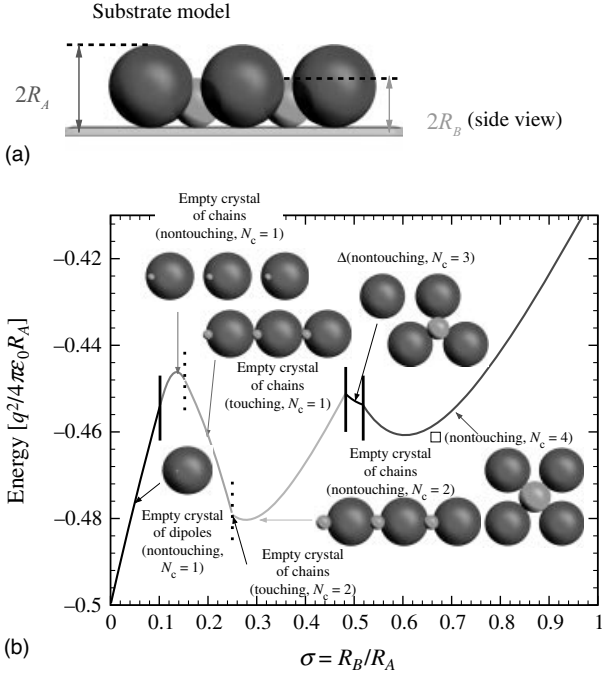
Figure 7. Stable structures of oppositely charged spheres versus their size asymmetry $\sigma = R_B/R_A$ in the substrate model, where all sphere surfaces touch the same plane: **(a)** side view, **(b)** energy per ion (scaled). Discontinuous transitions between the structures are indicated by a solid bar. Continuous transitions are denoted by a broken bar. Bottom views of the unit cells of the corresponding stable phases are shown, where the big (small) have a radius R_A (R_B). (See the color version of this figure in Color Plates section.)

our calculations. More experimental investigations on systems with higher size asymmetry are required to see the $\triangle$(nontouching) and the predicted empty crystals of chains and dipoles. Our crystalline structures can also be verified for molecular salts. However, here a soft core description may be relevant, which can alter the phase diagram.

III.   EXPLORING THE THIRD DIMENSION: BUCKLING AND LAYERING TRANSITIONS

The third dimension is explored via an external potential $V_{\text{ext}}(z)$ that confines the particles to a planar layer where z is the coordinate perpendicular to the layer. There are several models for this confining potential, and two of them have been considered in more detail, namely, hard slit confinement and parabolic (or harmonic) confinement. The hard slit confinement just involves geometric constraints

and contains no energy scale. In this case, $V_{\text{ext}}(z)$ reads as

$$V_{\text{ext}}(z) = \begin{cases} \infty & \text{if } -L/2 \leq z \leq L/2 \\ 0 & \text{else} \end{cases} \tag{7}$$

if the confining walls are located at $z = \pm L/2$, where L is the total (effective) slit width. In the parabolic case, on the other hand,

$$V_{\text{ext}}(z) = \frac{1}{2} K_0 z^2 \tag{8}$$

The amplitude K_0 involves an energy scale. Furthermore, charged colloids between charged plates experience a screened Coulomb interaction potential such that

$$V_{\text{ext}}(z) = V_0 \cosh(\kappa z) \tag{9}$$

is a reasonable approximation for this situation [62]. For small z, Eq. (9) obviously reduces to the parabolic form (8).

In the sequel, we shall describe results for hard spheres in a hard slit and for Yukawa particles in a hard slit. We then turn to parabolic confinements.

A.   Hard Spheres Between Hard Plates

Hard spheres confined between two slits constitute the simplest nontrivial model system for exploring the third dimension since temperature is irrelevant for hard interactions. Hence, there are only two parameters characterizing the system, namely, the slit width L and the packing fraction. The latter can be expressed in terms of a rescaled number density per area, N/A, as

$$\rho^* = \frac{N}{AL} \sigma^3 \tag{10}$$

where σ is the hard sphere diameter. Note that ρ^* is dimensionless. It is also convenient to introduce a scaled (dimensionless) slit width

$$h = (L - \sigma)/\sigma \tag{11}$$

such that $h = 0$ is the pure two-dimensional situation of perfect confinement. The quantity ρ^* varies between 0 and close packing. For increasing h, the following cascade of close-packed configurations is obtained [17–19]:

$$1\triangle \rightarrow b \rightarrow 2\square \rightarrow r \rightarrow 2\triangle \tag{12}$$

These corresponding structures are shown in Fig. 8. In Eq. (12), $1\triangle$ is a triangular (or hexagonal) monolayer and b denotes a buckled phase of linear arrays of spheres
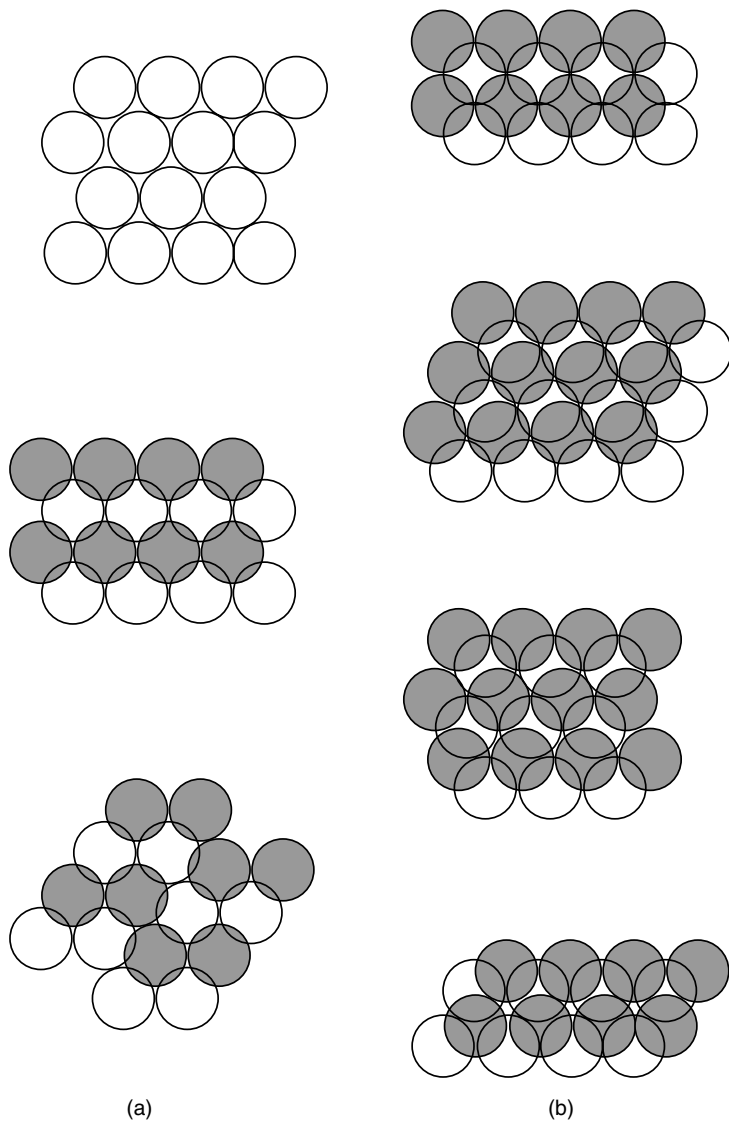
Figure 8. The various close-packed structures. **(a)** 1△, linear buckling, and zigzag buckling. **(b)** 2□, linear rhombic, zigzag rhombic, and 2△ (from top to bottom). Spheres from the lower layer are dark shaded, while spheres from the upper layer are transparent.
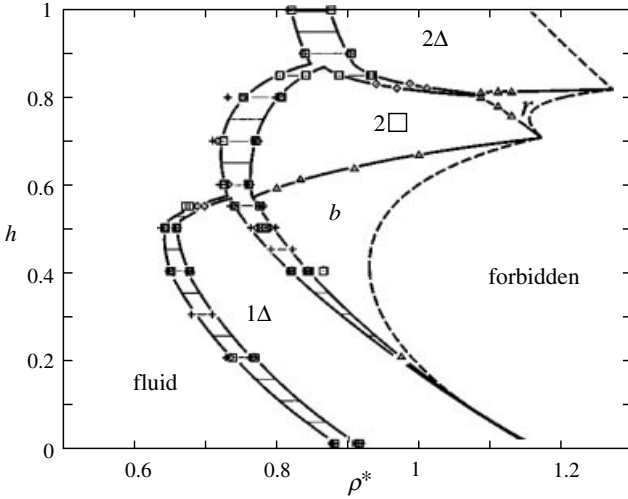
Figure 9. Monte Carlo result for the phase diagram of hard spheres of density ρ^* confined between parallel plates with separation distance h for different total particle numbers $N = 192(+)$; $384, 512(\diamond)$; $576(\triangle)$; and $1024, 1156(\square)$. Solid lines are a guide to the eye. Thin horizontal lines represent two-phase coexistence.

having a perpendicular zigzag structure. Then two intersecting square layers are stable, which is denoted by $2\square$. This configuration shears upon further increased h via the rhombic phase r until a situation of two staggered triangular layers occurs, which is called $2\triangle$ structure (see Fig. 8).

Beyond the bilayer regime limited by $2\triangle$, the cascade is even more complicated [63, 64]:

$$2\triangle \rightarrow \text{2hcp-like} \rightarrow \text{2hcp(100)} \rightarrow \text{2hcp-like} \rightarrow 2P_\square \rightarrow 3\square \qquad (13)$$

and involves a prism phase ($P_\square$) and more complicated cutouts and derivations from the hcp phase [64–66]. All the corresponding structures have been confirmed in experiments in the limit of high salt concentration [64, 65, 67–69].

In the regime of small h, the phase diagram in the (ρ^*, h) plane is shown in Fig. 9. There is only a small stability regime for the rhombic phase. Exploring the phase diagram beyond the $2\triangle$ phase away from close packing is still an open question.

B. Yukawa Particles Between Hard Walls

At zero temperature, the stable crystalline structure for Yukawa particles in a hard slit was obtained for various screening strengths and densities. It is now convenient to introduce the two dimensionless parameters characterizing the system, namely,

a reduced screening constant

$$\lambda = \kappa L \qquad (14)$$

and a reduced two-dimensional number density

$$\eta = \frac{N}{2A} L^2 \qquad (15)$$

Here, $\lambda = 0$ corresponds to the unscreened Coulomb system [70–74], while the hard sphere case is obtained in the opposite limit $\lambda \to \infty$. Dusty plasmas represent another realization for Yukawa bilayers. Here, static and dynamical correlations were simulated and analyzed [75, 76].

In the bilayer regime, the phase diagram was obtained in Refs. [77, 78] and is shown in Fig. 10. The phases $1\triangle$, b, $2\square$, $2\triangle$, known from the hard sphere case, are also present at finite screening. However, there is an additional rhombic phase with a reentrant behavior (see Fig. 10), called IVA, that is missing for the hard spheres. Experiments on charged suspensions [64, 79] have confirmed the bilayer phase diagram [80].

Solvation force experiments provides an alternative access to freezing phenomena of confined charged suspensions [81]. The regime beyond bilayers was explored more recently [63] and a complex transition scenario from the $2\triangle$ to the $3\square$ layered phase was found. This is shown in Fig. 11. Apart from two prism phases $P_\triangle$ and $P_\square$ with triangular or square bases, a 2hcp-like and a 2hcp(100) phase are stable. Furthermore, there is a double-buckle structure that is reminiscent to a Belgian waffle iron and is therefore called *BWI* (Belgian waffle iron). Some of these additional phases have been confirmed experimentally [64, 67], but not all. In particular, the *BWI* phase still needs experimental verification. Finally, we mention that finite temperatures were also explored in Monte Carlo simulations [82].

C.   Charged Particles in a Charged Slab

A parabolic confinement [83, 84] leads to stable structures that are different from those known from hard slit confinement. In general, a parabolic confinement tends to keep more particles to the central part of the slit. A special model for parabolic confinement was recently considered in Ref. [85]. Here, the counterions of confined macroions were smeared out homogeneously across the slit. This leads to a parabolic confining potential

$$V_{\text{ext}}(z) = \begin{cases} \dfrac{\eta q}{\epsilon_0 \epsilon L^3} z^2 & \text{for} -L/2 \le z \le L/2 \\[3mm] \dfrac{\eta q}{\epsilon_0 \epsilon L^2} |z| - \dfrac{\pi \eta q}{4\epsilon_0 \epsilon L} & \text{else} \end{cases} \qquad (16)$$
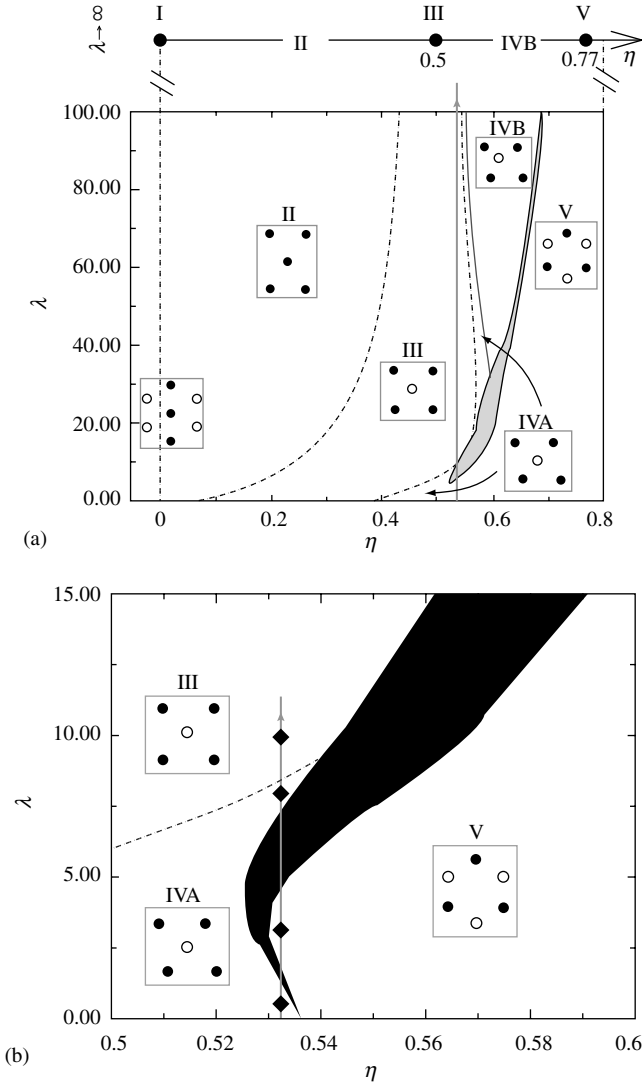
Figure 10.   Phase diagram of the Yukawa bilayer in the (η, λ) plane. **(a)** The hard sphere limit $\lambda \to \infty$ is shown on top. The dashed (solid) lines denote continuous (discontinuous) transitions. The filled region corresponds to the coexistence domain of phases IV and V. The vertical arrow indicates the double reentrant behavior of phase IVA. The insets show the lattice geometries, where the filled (open) circles correspond to the lower (upper) layer. **(b)** Magnification of **(a)** showing a reentrant behavior of phase IVA occurring at moderate λ. The four diamonds along the arrow indicate state points that show reentrant behavior. Adapted from Ref. [77]. (See the color version of this figure in Color Plates section.)
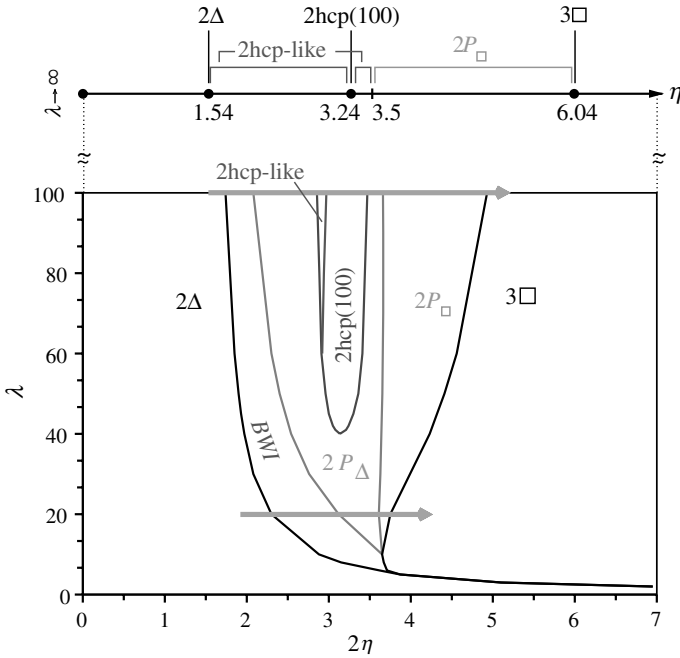
Figure 11. Zero-temperature phase diagram of a Yukawa system confined between two hard plates with screening strength λ and reduced density η in the multilayer regime between two triangular and three square layers. Stability regions of the Belgian waffle iron (BWI) phase, prism phases with triangular ($2P_\triangle$) and square bases ($2P_\square$), and 2hcp-like and 2hcp(100) phases are shown. For comparison, the hard-sphere limit of infinite screening is shown separately at the top. The arrows indicate a path of constant screening with increasing density. (See the color version of this figure in Color Plates section.)

where ϵ is the dielectric constant of the solvent, q is the macroion charge, and $\eta = NL^2/2A$ is the reduced number density. For increasing density η, the cascade of stable phases is shown in Fig. 12. In detail, the cascade is

$$1\triangle \rightarrow 3\triangle \rightarrow 2\square \rightarrow 2R \rightarrow 2\triangle \rightarrow 3\square \rightarrow 3R \rightarrow$$
$$3\triangle \rightarrow 4\square \rightarrow 4R \rightarrow 4\triangle \rightarrow 5R \rightarrow 5\triangle \rightarrow 6R \cdots \quad (17)$$

Here, $3R$, $4R$, $5R$, and $6R$ denote rhombic phases with 3, 4, 5, and 6 layers and with the stacking sequence ABA, $ABAB$, $ABABA$, and $ABABAB$, whereas the triangular phases $3\triangle$, $4\triangle$, and $5\triangle$ occur with a stacking sequence ABC, $ABCA$, and $ABCAB$, respectively. Figure 12 shows the maximal interlayer spacing D, that is, the distance between the two outermost layers, versus density. Remarkably, the buckling transition from a monolayer occurs into a trilayer structure $3\triangle$. This is in marked contrast to the hard slit, where buckling occurred into a bilayer with a
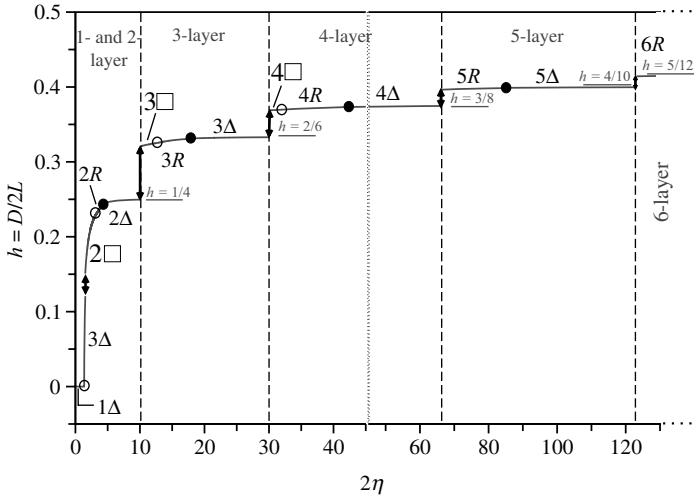
Figure 12. Order parameter h of all stable crystalline phases. Empty circles denote a continuous transition, while the full circles mark a discontinuous one. The transitions between different layer numbers, rendered as dashed lines, are also recorded as a first-order transition except $1\triangle \rightarrow 3\triangle$. Apart of that, the underlined h numbers give the limit h value ($\eta \rightarrow \infty$), for the case that no more phase transition to a higher layered structure occurs. The dotted line indicates a scale change in η-axis.

rectangular unit cell. As a remark, a third possibility of buckling that was predicted in Landau expansions [86] and discovered in Lennard-Jones systems [87] is an asymmetric bilayer. All three structures are summarized in Fig. 13. However, the buckling both into a trilayer and into the asymmetric structure still needs experimental confirmation. Clearly, more work is needed to map out the stability of various buckled structures for different parabolic confinements.

IV.   CONCLUSIONS

In conclusion, we have summarized recent progress made by theory, computer simulation, and experiment for colloidal crystallization between two and three dimensions. In particular, a strictly two-dimensional binary system was considered. For increasing asymmetry between the two species, the stable crystalline structures were getting more complex and involved mainly triangular, square, and rhombic bases, sometimes with complicated unit cells. Explicit results were discussed for hard disks as well as for dipolar and Yukawa interactions and oppositely charged mixtures. Theoretical predictions were compared to experiments, in particular to superparamagnetic particles at a pending air–water interface and to oppositely charged granulates on a table.
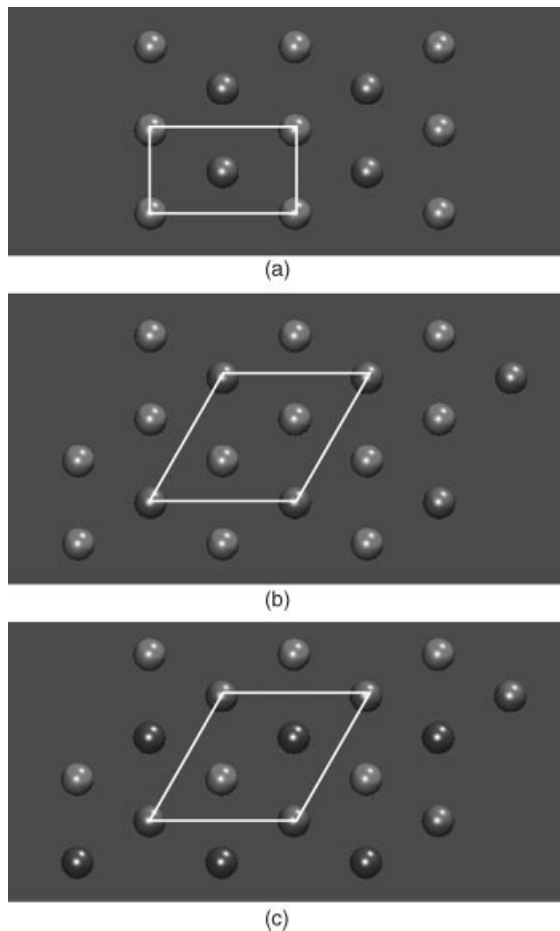
Figure 13. Top views of the buckled structures starting from a triangular confined monolayer. **(a)** symmetric 1-1 rows with a 2×1 structure, **(b)** 2-1 structure with a $\sqrt{3} \times \sqrt{3}$ corrugation, and **(c)** 1-1-1 trilayer ($3\triangle$). Particles in different layers are indicated by different colors. White lines denote primitive unit cell of each structure. (See the color version of this figure in Color Plates section.)

Then, a slit-like confinement was considered and buckling and layering transitions were described for one-component systems, such as hard spheres and Yukawa particles, both in hard-slit and harmonic (parabolic) confinement potentials. Here, a comparison of the theoretical calculations can be done to real-space experiments of charged colloids confined between two glass plates. There are, however, multilayered structures that have not yet been confirmed experimentally.

Future research is expected to cover the following directions. First, it would be interesting to study *anisotropic particle* interactions. These can describe anisotropic particles with a fixed orientation or orientable particles with additional rotational degrees of freedom. Possible examples include apolar hard anisotropic particles such as spherocylinders [88, 89], ellipsoids [90] or cubes [91], and Yukawa

segment rods [92–94]. Also, polar particles can be considered including dipoles with their moment lying in the plane [95, 96] or tilted relative to the plane [97–100]. Furthermore, chains composed of individual dipoles can be considered [101].

There are only few studies of two-dimensional binary mixtures of nonspherical particles [102, 103] revealing already interesting phase behavior. Owing to the additional degrees of freedom more complicated crystalline solids are expected, leading to a wealth of new phenomena that should be explored in the future.

On the other hand, there are more studies on one component of anisotropic particles in confinement, most of them in the fluid state [104–106]. The crystalline state is much less explored under strong confinement. For instance, the close-packed configuration of orientable hard spherocylinders in hard-slit confinement is not yet known. Also, the glass transition for anisotropic confined particles [107, 108] needs a better understanding.

A second line of research for the future is the inclusion of *gravity*. Gravity can be experimentally realized by simply tilting the sample or by imposing an external light pressure field [109]. If gravity is acting in the plane of a binary crystalline monolayer, increasing the position coordinate relative to the gravity direction corresponds to an isothermal path in the plane spanned by the two chemical potentials [110]. This may result in an unexpected phase sequence for increasing height. For instance, a floating liquid layer was identified in a colloid–polymer mixture [111]. If gravity, on the other hand, acts perpendicular to a confining slit plane, the up–down symmetry is broken. Gravity shifts the buckling transition from second to first order [112]. It will also induce asymmetric layering situations and will therefore create a new scenario of layering.

Acknowledgments

References

1. S. M. Woodley and R. Catlow, *Nat. Mater.*, **7**, 937 (2008).
2. L. Filion, M. Marechal, B. van Oorschot, D. Pelt, F. Smallenburg, and M. Dijkstra, *Phys. Rev. Lett.*, **103**, 188302 (2009).
3. M. O. Robbins, K. Kremer, and G. S. Grest, *J. Chem. Phys.*, **88**, 3286 (1988).
4. H. Löwen, *Phys. Rep.*, **237**, 249 (1994).
5. S. Prestipino, F. Saija, and G. Malescio, *Soft Matter*, **5**, 2795 (2009).
6. G. Malescio and G. Pellicane, *Nat. Mater.*, **2**, 97 (2003).
7. C. N. Likos, M. Watzlawek, and H. Löwen, *Phys. Rev. E*, **58**, 3135 (1998).
8. P. Bolhuis and D. Frenkel, *Phys. Rev. Lett.*, **72**, 2211 (1994).
9. P. Bolhuis and D. Frenkel, *J. Phys. Condens. Matter*, **9**, 381 (1997).
10. C. N. Likos, Z. T. Németh, and H. Löwen, *J. Phys. Condens. Matter*, **6**, 10965 (1994).

11. A. R. Denton and H. Löwen, *J. Phys. Condens. Matter*, **9**, L1 (1997).

12. P. M. Chaikin and T. C. Lubensky, *Principles of Condensed Matter Physics*, 4th ed., Cambridge University Press, Cambridge, 1986.

13. L. Bonsall and A. A. Maradudin, *Phys. Rev. B*, **15**, 1959 (1977).

14. J. Fröhlich and C. Pfister, *Commun. Math. Phys.*, **81**, 277 (1981).

15. C. N. Likos and C. L. Henley, *Philos. Mag.*, B **68**, 85 (1993).

16. K. Franzrahe and P. Nielaba, *Phys. Rev. E*, **79**, 051505 (2009).

17. P. Pieranski, L. Strzelecki, and B. Pansu, *Phys. Rev. Lett.*, **50**, 900 (1983).

18. M. Schmidt and H. Löwen, *Phys. Rev. Lett.*, **76**, 4552 (1996).

19. M. Schmidt and H. Löwen, *Phys. Rev. E*, **55**, 7228 (1997).

20. G. E. Morfill and A. V. Ivlev, *Rev. Mod. Phys.*, **81**, 1353 (2009).

21. K. Zahn, J. M. Mendez-Alcaraz, and G. Maret, *Phys. Rev. Lett.*, **79**, 175 (1997).

22. K. Zahn, R. Lenke, and G. Maret, *Phys. Rev. Lett.*, **82**, 2721 (1999).

23. K. Zahn and G. Maret, *Phys. Rev. Lett.*, **85**, 3656 (2000).

24. M. Köppl, P. Henseler, A. Erbe, P. Nielaba, and P. Leiderer, *Phys. Rev. Lett.*, **97**, 208302 (2007).

25. K. Mangold, J. Birk, P. Leiderer, and C. Bechinger, *Phys. Chem. Chem. Phys.*, **6**, 1623 (2004).

26. M. Kollmann, R. Hund, B. Rinn, G. Nagele, K. Zahn, H. König, G. Maret, R. Klein, and J. K. G. Dhont, *Europhys. Lett.*, **58**, 919 (2002).

27. N. Hoffmann, F. Ebert, C. N. Likos, H. Löwen, and G. Maret, *Phys. Rev. Lett.*, **97**, 078301 (2006).

28. N. Hoffmann, C. N. Likos, and H. Löwen, *J. Phys. Condens. Matter*, **18**, 10193 (2006).

29. H. König, R. Hund, K. Zahn, and G. Maret, *Eur. Phys. J. E*, **18**, 287 (2005).

30. P. A. Trasca and S. H. L. Klapp, *J. Chem. Phys.*, **129**, 084702 (2008).

31. J. Jordanovic and S. H. L. Klapp, *Phy. Rev. Lett.*, **101**, 038302 (2008).

32. C. Holm and J. J. Weis, *Curr. Opin. Colloid Interface Sci.*, **10**, 133 (2005).

33. J.-P. Hansen and I. R. MacDonald, *Theory of Simple Liquids*, 2nd ed. Academic, New York, 1986.

34. M. B. Hay, R. K. Workman, and S. Manne, *Phys. Rev. E*, **67**, 012401 (2003).

35. L. Assoud, R. Messina, and H. Löwen, *Europhys. Lett.*, **80**, 48001 (2007).

36. J. Fornleitner, F. Lo Verso, G. Kahl, and C. N. Likos, *Soft Matter*, **4**, 480 (2008).

37. L. Assoud, F. Ebert, P. Keim, R. Messina, G. Maret, and H. Löwen, *J. Phys. Condens. Matter*, **21**, 464114 (2009).

38. F. Ebert, P. Keim, and G. Maret, *Eur. Phys. J. E*, **26**, 161 (2008).

39. L. Assoud, F. Ebert, P. Keim, R. Messina, G. Maret, and H. Löwen, *Phys. Rev. Lett.*, **102**, 238301 (2009).

40. M. Bayer, J. M. Brader, F. Ebert, M. Fuchs, E. Lange, G. Maret, R. Schilling, M. Sperl, and J. P. Wittmer, *Phys. Rev. E*, **76**, 011508 (2007).

41. T. Hamanaka and A. Onuki, *Phys. Rev. E*, **75**, 041503 (2007).

42. A. Widmer-Cooper and P. Harrowell, *Phys. Rev. Lett.*, **96**, 185701 (2006).

43. T. Kawasaki, T. Araki, and H. Tanaka, *Phys. Rev. Lett.*, **99**, 215701 (2007).

44. E. Chang and D. Hone, *Europhys. Lett.*, **5**, 635 (1988).

45. R. Messina and H. Löwen, *Phys. Rev. Lett.*, **91**, 146101 (2003).

46. E. Allahyarov, I. D'Amico, and H. Löwen, *Phys. Rev. E*, **90**, 3199 (1999).

47. E. Allahyarov and H. Löwen, *J. Phys. Condens. Matter*, **21**, 1 (2009).

48. N. J. Lorenz, H. J. Schope, H. Reiber, T. Palberg, P. Wette, I. Klassen, D. Holland-Moritz, D. Herlach, and T. Okubo, *J. Phys. Condens. Matter*, **21**, 464116 (2009).

49. B. D'Aguanno, R. Krause, J. M. Mendez-Alcaraz, and R. Klein, *J. Phys. Condens. Matter*, **4**, 3077 (1992).

50. O. S. Vaulina, O. F. Petrov, A. V. Gavrikov, and V. E. Fortov, *Plasma Phys. Rep.*, **33**, 278 (2007).

51. L. Assoud, R. Messina, and H. Löwen, *J. Chem. Phys.*, **129**, 164511 (2008).

52. A. P. Hynninen, C. G. Christova, R. van Roij, A. van Blaaderen, and M. Dijkstra, *Phys. Rev. Lett.*, **96**, 138308 (2006).

53. A. P. Hynninen, M. E. Leunissen, A. van Blaaderen, and M. Dijkstra, *Phys. Rev. Lett.*, **96**, 018303 (2006).

54. J. J. Weis, D. Levesque, and J. M. Caillol, *J. Chem. Phys.*, **109**, 7486 (1998).

55. A. V. Fiacco and G. P. McCormick, *Nonlinear Programming: Sequential Unconstrained Minimization Technique*, Wiley, New York, 1968.

56. L. Assoud, R. Messina, and H. Löwen, *Europhys. Lett.*, **89**, 36001 (2010).

57. M. E. Leunissen, C. G. Christova, A. P. Hynninen, C. P. Royall, A. I. Campbell, A. Imhof, M. Dijkstra, R. van Roij, and A. van Blaaderen, *Nature*, **437**, 235 (2005).

58. C. E. McNamee, M. Jaumann, M. Moller, A. L. Ding, S. Hemeltjen, S. Ebert, W. Baumann, and W. A. Goedel, *Langmuir*, **21**, 10475 (2005).

59. G. K. Kaufman, S. W. Thomas, M. Reches, B. F. Shaw, J. Feng, and G. M. Whitesides, *Soft Matter*, **5**, 1188 (2009).

60. G. K. Kaufman, M. Reches, S. W. Thomas, B. F. Shaw, J. Feng, and G. M. Whitesides, *App. Phys. Lett.*, **94**, 044102 (2009).

61. P. Hartmann, Z. Donko, and J. Kalman, *Europhys. Lett.*, **72**, 396 (2005).

62. D. Andelman, *Handbook of Biological Physics*, R. Lipowsky and E. Sackmann, eds., Elsevier, 1995.

63. E. C. Oğuz, R. Messina, and H. Löwen, *Europhys. Lett.* **86**, 28002 (2009).

64. F. Ramiro-Manzano, E. Bonet, I. Rodriguez, and F. Meseguer, *Phys. Rev. E*, **76**, 050401(R) (2007).

65. S. Neser, C. Bechinger, P. Leiderer, and T. Palberg, *Phys. Rev. Lett.*, **79**, 2348 (1997).

66. A. Fortini and M. Dijkstra, *J. Phys. Condens. Matter*, **18**, 371 (2006).

67. F. Ramiro-Manzano, F. Meseguer, E. Bonet, and I. Rodriguez, *Phys. Rev. Lett.*, **97**, 028304 (2006).

68. F. R. Manzano, E. Bonet, I. Rodriguez, and F. Meseguer, *Soft Matter*, **5**, 4279 (2009).

69. I. Cohen, T. G. Mason, and D. A. Weitz, *Phy. Rev. Lett.*, **93**, 046001 (2004).

70. G. Goldoni and F. M. Peeters, *Phys. Rev. B*, **53**, 4591 (1998).

71. G. Goldoni and F. M. Peeters, *Phy. Rev. B*, **53**, 4591 (1998).

72. I. V. Schweigert, V. A. Schweigert, and F. M. Peeters, *Phy. Rev. B*, **60**, 14665 (1999).

73. I. V. Schweigert, V. A. Schweigert, and F. M. Peeters, *Phy. Rev. Lett.*, **82**, 5293 (1999).

74. R. Messina, *J. Phys. Condens. Matter*, **21**, 113102 (2009).

75. H. Baumgartner, D. Block, and M. Bonitz, *Contrib. Plasma Phys.*, **49**, 281 (2009).

76. Z. Donko, P. Hartmann, G. J. Kalman, and K. I. Golden, *J. Phys. A*, **36**, 5877 (2003).

77. R. Messina and H. Löwen, *Phys. Rev. Lett.*, **91**, 146101 (2003).

78. R. Messina and H. Löwen, *Phys. Rev. E*, **73**, 011405 (2006).

79. A. B. Fontecha, T. Palberg, and H. J. Schöpe, *Phys. Rev. E*, **76**, 050402(R) (2007).

80. A. B. Fontecha, H. J. Schöpe, H. König, T. Palberg, R. Messina, and H. Löwen, *J. Phys. Condens. Matter*, **17**, S2779 (2005).

81. S. H. L. Klapp, Y. Zeng, D. Qu, and R. von Klizing, *Phy. Rev. Lett.*, **100**, 118303 (2008).

82. S. Grandner and S. H. L. Klapp, *J. Chem. Phys.*, **129**, 244703 (2008).

83. H. Totsuji, T. Kishimoto, and C. Totsuji, *Phys. Rev. Lett.*, **78**, 3113 (1997).

84. H. Totsuji and J. L. Barrat, *Phys. Rev. Lett.*, **60**, 2484 (1988).

85. E. C. Oğuz, R. Messina, and H. Löwen, *J. Phys. Condens. Matter*, **21**, 424110 (2009).

86. T. Chou and D. R. Nelson, *Phys. Rev. E*, **48**, 4611 (1993).

87. H. Bock, K. E. Gubbins, and K. G. Ayappa, *J. Chem. Phys.*, **122**, 094709 (2005).

88. P. Bolhuis and D. Frenkel, *J. Chem. Phys.*, **106**, 666 (1997).

89. H. Löwen, *Phys. Rev. E*, **50**, 1232 (1994).

90. D. Frenkel, B. M. Mulder, and J. P. McTague, *Phys. Rev. Lett.*, **52**, 287 (1984).

91. B. Groh and B. Mulder, *J. Chem. Phys.*, **114**, 3653 (2001).

92. H. Löwen, *J. Chem. Phys.*, **100**, 6738 (1994).

93. T. Kirchhoff, H. Löwen, and R. Klein, *Phys. Rev. E*, **53**, 5011 (1996).

94. H. H. Wensink and H. Löwen, *Phys. Rev. E*, **78**, 031409 (2008).

95. E. Lomba, F. Lado, and J. J. Weis, *Phys. Rev. E*, **61**, 3838 (2000).

96. V. A. Froltsov and S. H. L. Klapp, *J. Chem. Phys.*, **126**, 114703 (2007).

97. V. A. Froltsov, R. Blaak, C. N. Likos, and H. Löwen, *Phys. Rev. E*, **68**, 061406 (2003).

98. V. A. Froltsov, C. N. Likos, H. Löwen, C. Eisenmann, U. Gasser, P. Keim, and G. Maret, *Phys. Rev. E*, **71**, 031404 (2005).

99. C. Eisenmann, U. Gasser, P. Keim, and G. Maret, *Phys. Rev. Lett.*, **93**, 105702 (2004).

100. A. Chremos and C. N. Likos, *J. Phys. Chem. B*, **113**, 12316 (2009).

101. Y. Terada and M. Tokuyama, *J. Phys. Soc. Jap.*, **78**, 084803 (2009).

102. A. Stroobants, *Phys. Rev. Lett.*, **69**, 2388 (1992).

103. A. Stroobants, *J. Phys. Condens. Matter*, **6**, A285 (1994).

104. M. Dijkstra and R. van Roij, *J. Phys. Condens. Matter*, **17**, S3507 (2005).

105. Y. Trukhina and T. Schilling, *Phys. Rev. E*, **77**, 011701 (2008).

106. M. Gramzow and S. H. L. Klapp, *Phys. Rev. E*, **75**, 011605 (2007).

107. A. Latz, M. Letz, R. Schilling, and T. Theenhaus, *J. Non-Cryst. Solids*, **307**, 172 (2002).

108. C. Renner, H. Löwen, and J. L. Barrat, *Phys. Rev. E*, **52**, 5091 (1995).

109. M. C. Jenkins and S. U. Egelhaaf, *J. Phys. Condens. Matter*, **20**, 404220 (2008).

110. J. Dzubiella, H. M. Harreis, C. N. Likos, and H. Löwen, *Phys. Rev. E*, **64**, 011405 (2001).

111. M. Schmidt, M. Dijkstra, and J. P. Hansen, *Phys. Rev. Lett.*, **93**, 088303 (2004).

112. H. Löwen, *Soft Matter*, **6**, 3133 (2010).